Supplementary Information (SI) for Inorganic Chemistry Frontiers.
This journal is © the Partner Organisations 2025

Supporting information

High density facet junctions in nano-stepped $CuFeO_2$ mediated efficient charge separation for selective photocatalytic CO_2 reduction to CH_4

Jingying Wei, Chun Guo, Dongfen Hou, Dailing Jia, Huaiguo Xue, Jingqi Tian, Tengfei Jiang.*

School of Chemistry and Chemical Engineering, Yangzhou University, 180 Siwangting Road, Yangzhou 225002, People's Republic of China

Corresponding Author Email: jiangtengfei@yzu.edu.cn

EXPERIMENTS:

Preparation of the $CuFeO_2$ Nanosheet. The $CuFeO_2$ nanosheet was prepared by the hydrothermal method based on our previous work. Measure 1 mmol $CuSO_4·5H_2O$ and 1 mmol $FeSO_4·7H_2O$ and dissolve them in 10 mL deionized water by ultrasound until dissolved, denoted as solution A; 10 mL Carboxymethyl chitosan aqueous solution with a concentration of 7 g/L was prepared and denoted as solution B; Dissolve 100 mmol NaOH in 10ml deionized water, denoted as solution C. Mixed solution A and B, the Carboxymethyl chitosan solution was evenly dispersed by mechanical stirring, transferred to the lining of the polytetrafluoroethylene reactor, and solution C was added as a mineralizing agent to obtain a brown suspension, which was heated at 160 °C for 6 h, centrifuged and washed with deionized water and ethanol, and dried at 80 °C for 12 h.

Preparation of stepped $CuFeO_2$ nanomaterials. Add 0.0304g $CuFeO_2$ into 40mL water and ultrasonic mixing evenly. 55 µL HCl was removed and added to the beaker and ultrasound was continued. Then the reaction liquid was transferred into the polytetrafluoroethylene reactor, reacted at 80 °C for 1 h, removed and washed with deionized water and ethanol, and dried at 60 °C for 12 h. The hydrochloric acid was added in amounts of 0, 53, 55, and 57 µL named CFO-E0, CFO-E1, CFO-E2, and CFO-E3, respectively.

Characterization.

Obtain SEM images using a Zeiss Supra 55 electron microscope; Obtain HRTEM and selected area electron diffraction images using a Tecnai G2 F30 S-TWIN transmission electron microscope operating at 200 kV, and perform EDX spectroscopy analysis to determine its surface elemental composition; Using a Bruker D8 focused diffractometer, XRD spectra of the product were recorded by Cu-K α radiation (λ=1.54178 Å) to characterize the crystal structure of the material. The diffraction angle (2 θ) ranged from 10-80 °, and the scanning rate was 10 ° min^{-1}; Obtain XPS spectra using ESCALAB 250 Xi Thermal Science X-ray Photoelectron Spectrometer and calibrate them by C 1s peak position; Using the Cary 5000 UV Vis NIR absorption spectrometer, absorbance images were obtained in the range of 200-2000 nm using an integrating sphere. The UV Vis images were processed using the Tauc plot method to obtain the indirect bandgap of the material; Obtain the N_2 adsorption desorption curve of the material using the Quadrasorb EVO physical adsorption instrument, calculate its specific surface area using the BET method, and measure the average pore size and pore volume; The fluorescence (PL) spectrum was recorded using an F-7000 FL spectrophotometer. Use Agilent 7890A-7697A headspace gas chromatograph with DB-WAX column to obtain the composition information of the liquid phase product of CO_2 reduction. In situ electrochemical attenuated total reflection surface-enhanced infrared absorption spectroscopy (ATR-SEIRAS) experiments were conducted on a Shimadzu IRXross FTIR spectrometer with silicon as the prismatic window at room temperature.

Fluorescence Microscopy Imaging.

Disperse the catalyst powder (10 mg) in 5 mL of water, sonicate for 30 minutes, take 10 µL of colloidal suspension and drop it onto a clean glass slide. Cover the glass slide and wait for the water to evaporate at room temperature to obtain a well dispersed catalyst particle layer. Then take 10 µL of 1 µM resazurin/amplex red aqueous solution and immerse it into the catalyst layer prepared above, carefully covering the droplets with a cover glass to prevent the formation of bubbles. Then, use the catalyst on the glass slide for fluorescence microscopy imaging. Please refer to [14] for specific details.

Photoelectrochemical measurements.

The photoelectrochemical responses of these photocatalysts were recorded on an Autolab electrochemical system using a 500-W xenon lamp with a light intensity of 100 mW/cm^2. The work electrodes were fabricated using a dip-coating method. A photocatalyst sample (8 mg) was added in ethylene glycol methyl ether (3 mL). The sample suspension was then dropped onto a fluorine-doped tin oxide substrate and dried by heating at 200 °C for 30 min under nitrogen atmosphere. Platinum wire and saturated Ag/AgCl were used as the counter electrode and reference electrode respectively in Na_2SO_4 (0.5 M) electrolytic solution to measure photoelectrochemical properties.

Photocatalytic performance test.

The photocatalytic reduction of CO_2 performance was tested in a closed system at atmospheric pressure and ambient temperature. First, 20 mg of photocatalyst particles, 0.1 M $NaHCO_3$ aqueous solution (9 mL) and 1mL TEOA(Trolamine) were placed into a quartz bottle with a volume of 25 mL. The suspension was then saturated with CO_2 by continuous bubbling with CO_2 gas for 15 min. The reaction time was 6 h under the irradiation of a xenon lamp with a light intensity of 100 mW/cm^2. Gas products were detected by gas chromatography (GC-211N, argon as carrier gas). The liquid products were determined by Agilent 7890A-7697A headspace gas chromatograph.

Photocatalytic oxidation of benzyl alcohol: The photocatalytic reaction was carried out in a quartz vial under air atmosphere by dispersing 10 mg of catalyst in 5 mL of DMF, 10 μL of benzyl alcohol, and adding 1.5 mg of KOH to provide an alkaline environment, with dodecane as the external standard. The light source was a 500 W xenon lamp with a light intensity of 100 mW/cm^2 and the reaction time was 4 h. The conversion and selectivity were determined by gas chromatography (GC-2014C).

Photocatalytic Reduction of Nitrobenzene: The photocatalytic reaction was carried out in a quartz vial under N_2 atmosphere by dispersing 10 mg of catalyst in 1 mL of hydrazine hydrate, 10 μL of nitrobenzene, and 5 mL of isopropanol with dodecane as the external standard. The light source was a 500 W xenon lamp with a light intensity of 100 mW/cm^2 and the reaction time was 6 h. The conversion and selectivity were determined by gas chromatography (GC-2014C).

RESULTS AND DISCUSSION

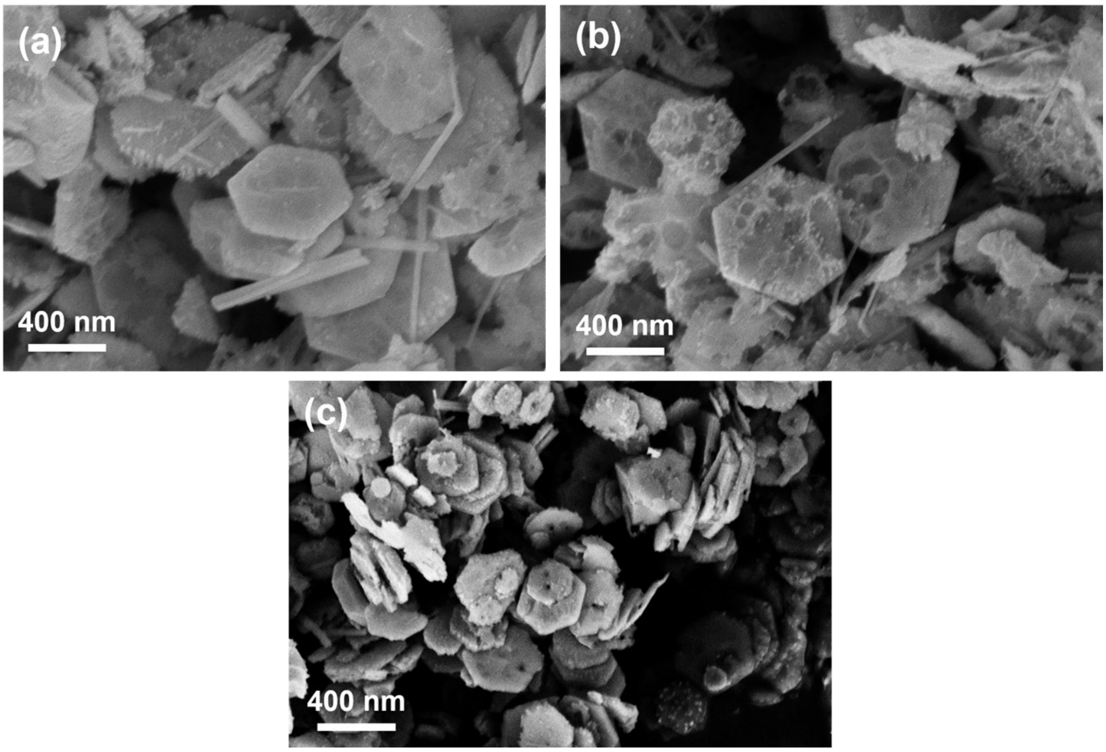

Fig. S1. Figures a-c show SEM images of CFO E1-E3, respectively.

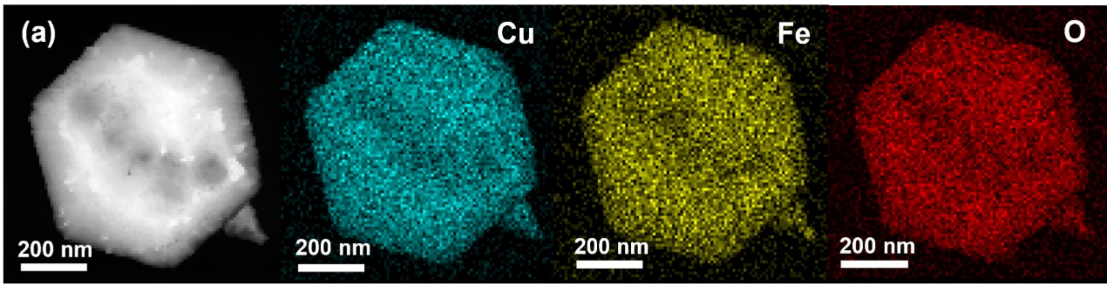

Fig. S2. (a) is the element distribution mapping image of CFO-E2.

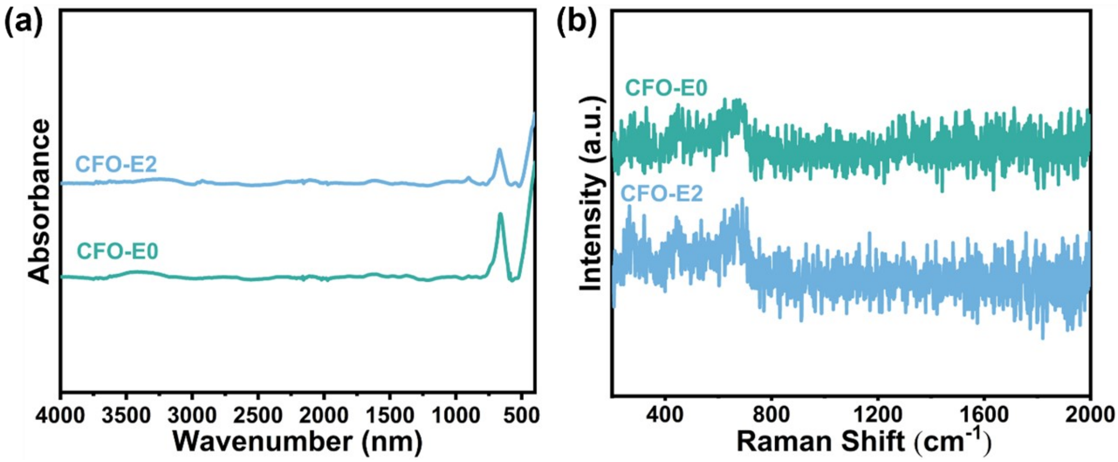

Fig. S3. FTIR spectra (a) and Raman spectra (b) of CFO-E0 and CFO-E2.

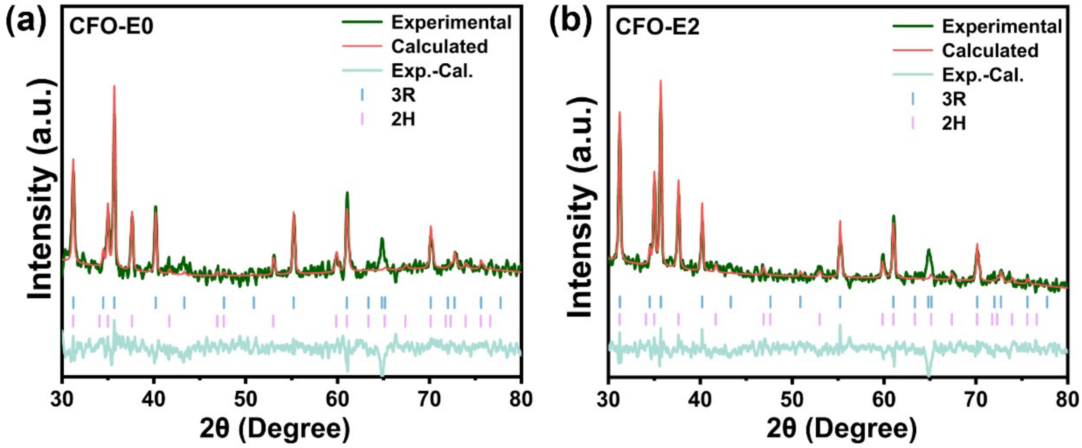

Fig. S4. Rietveld refinement of XRD patterns of CFO-E0 (a) and CFO-E2 (b).

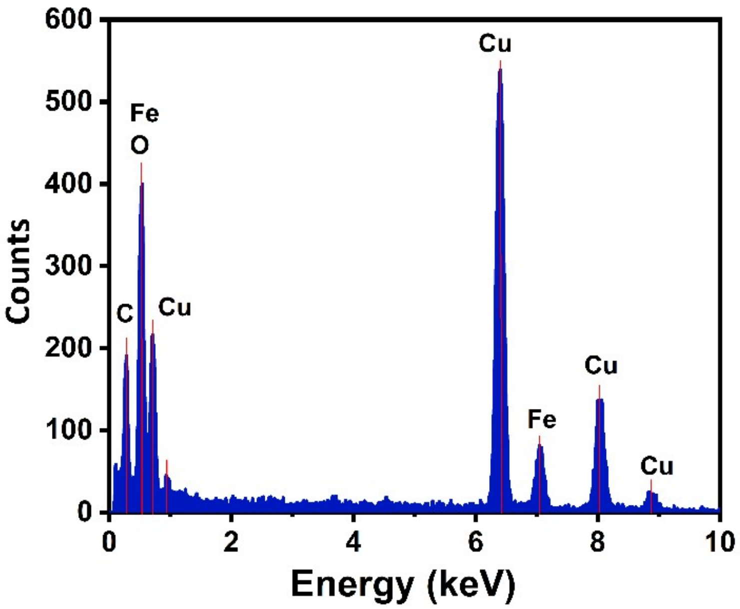

Fig. S5. EDS spectra of CFO-E2.

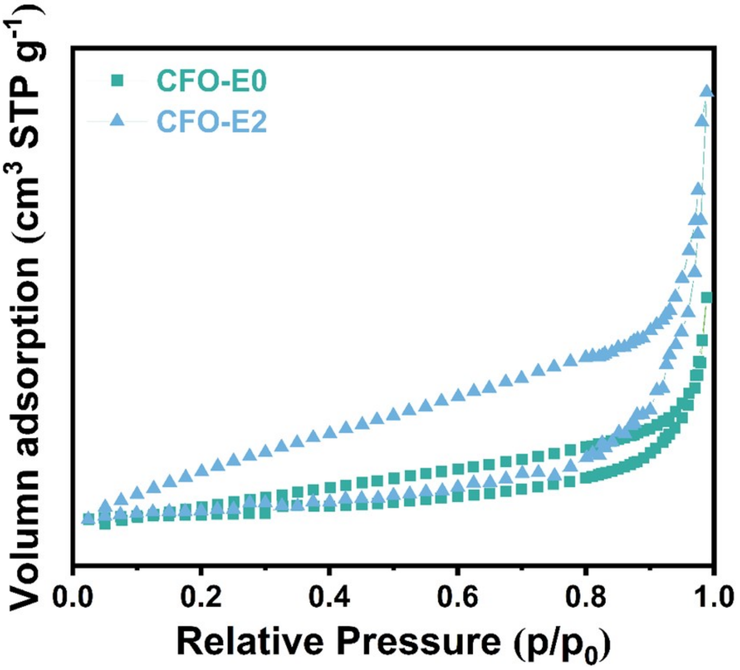

Fig. S6. N_2 adsorption desorption curves of CFO-E0 and CFO-E2

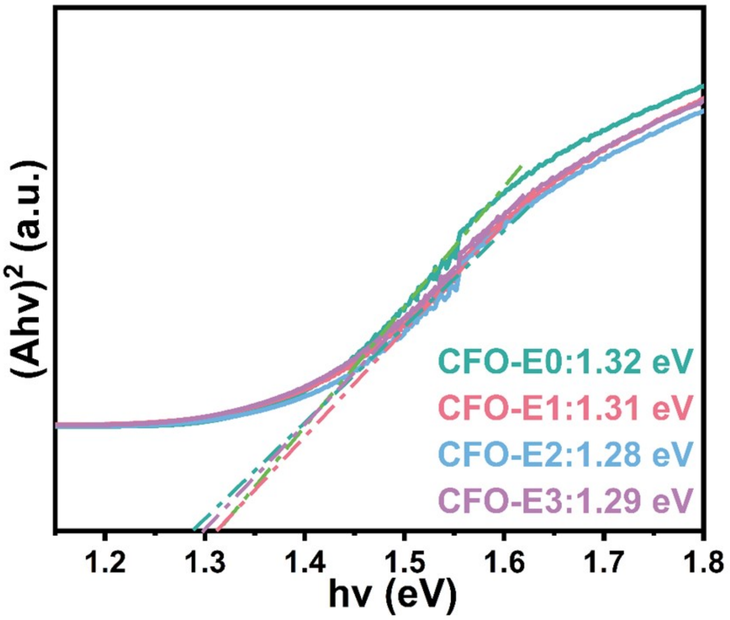

Fig. S7. Tauc plots of CFO E0-E3 from UV-vis-NIR spectra.

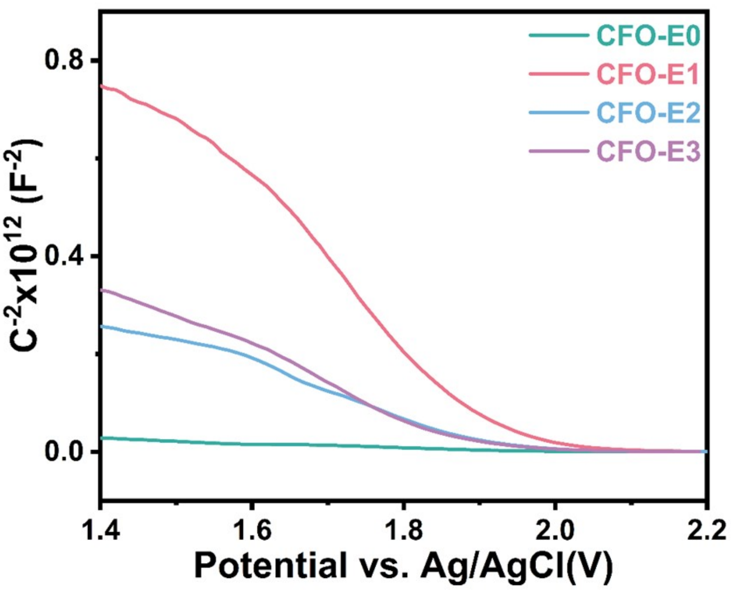

Fig. S8. Mott-Schottky plot in the dark state in 0.5 M Na_2SO_4 electrolyte.

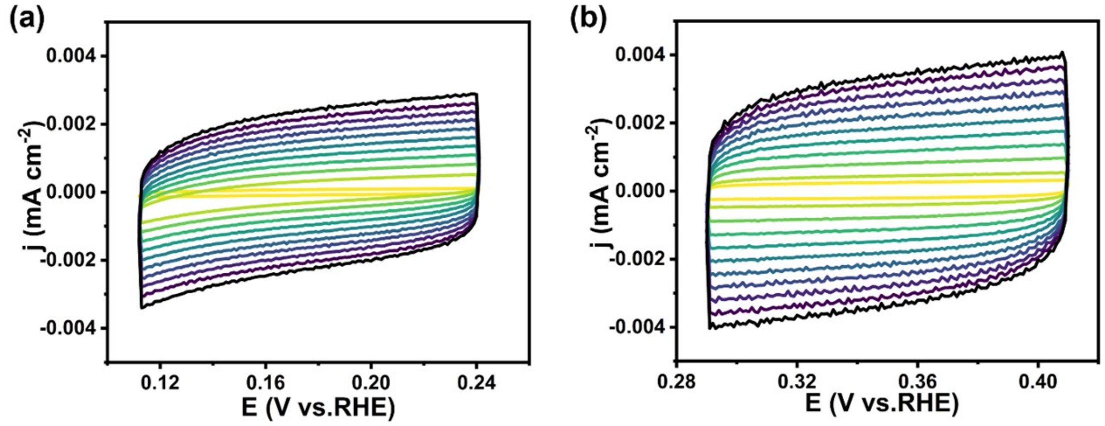

Fig. S9. (a) CVs of CFO-E0 and (b) CFO-E2 at scan rates of 10-200 mV s^{-1}.

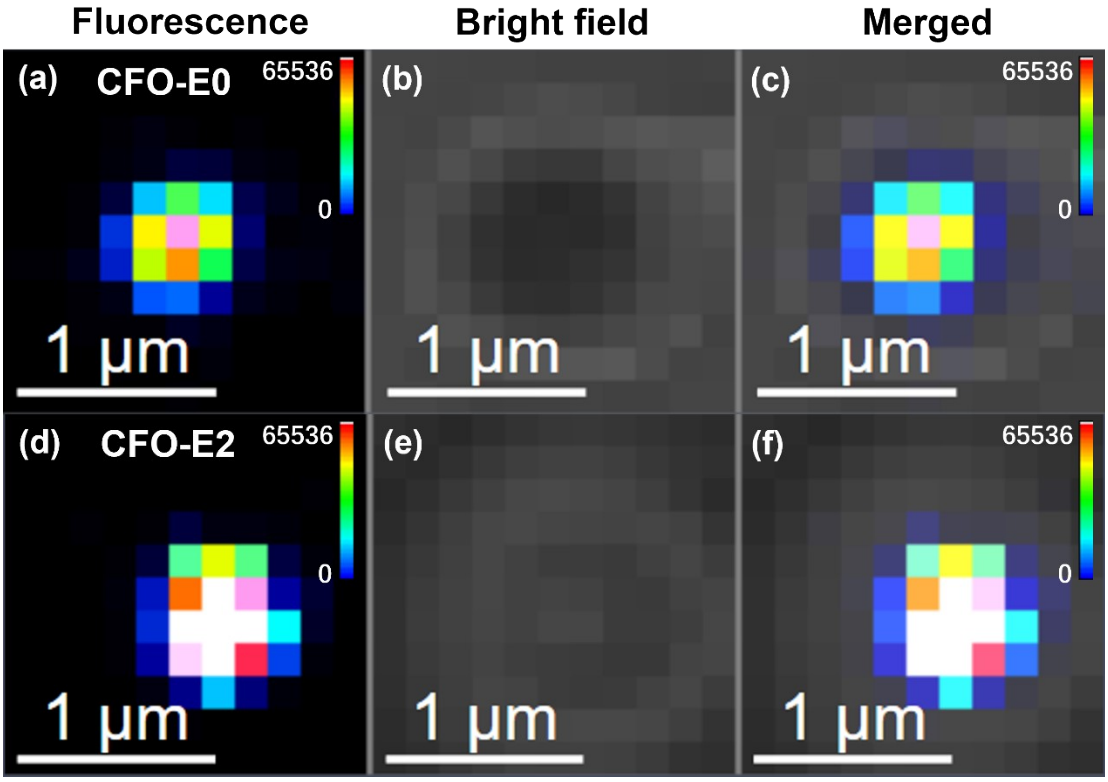

Fig. S10. Fluorescence microscopy images of CFO-E0 (a-c) and CFO-E2(d-f) in 1 μM resazurin.

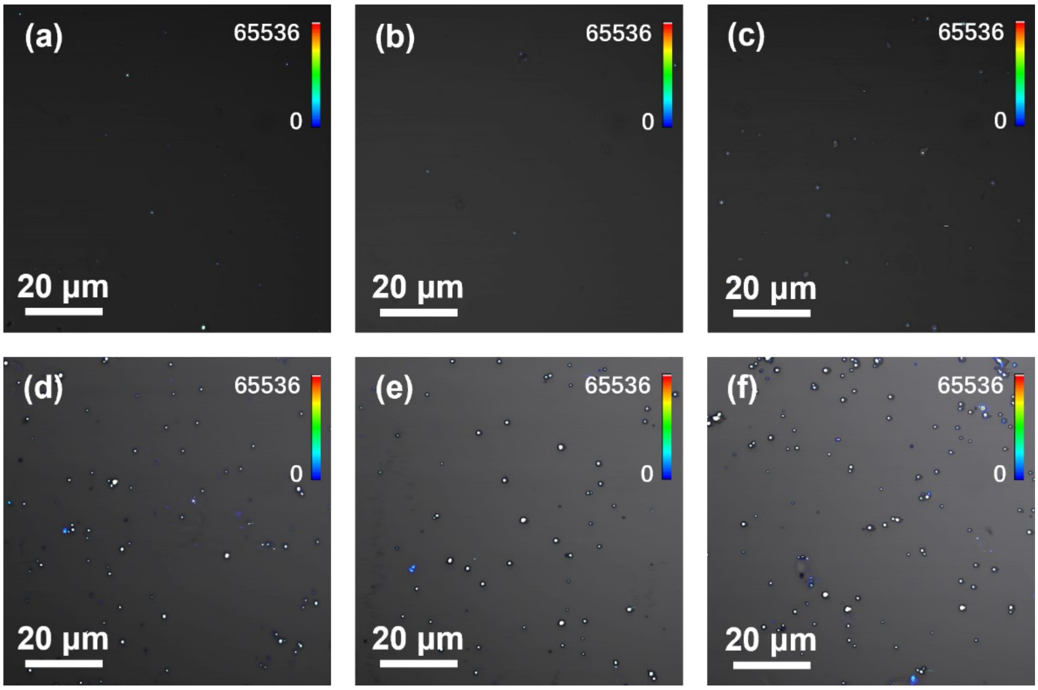

Fig. S11. Fluorescence microscopy images of CFO-E2 in 1 μM resazurin (a)-(h) and 1 μM amplex red (a)-(f) under different light intensities.

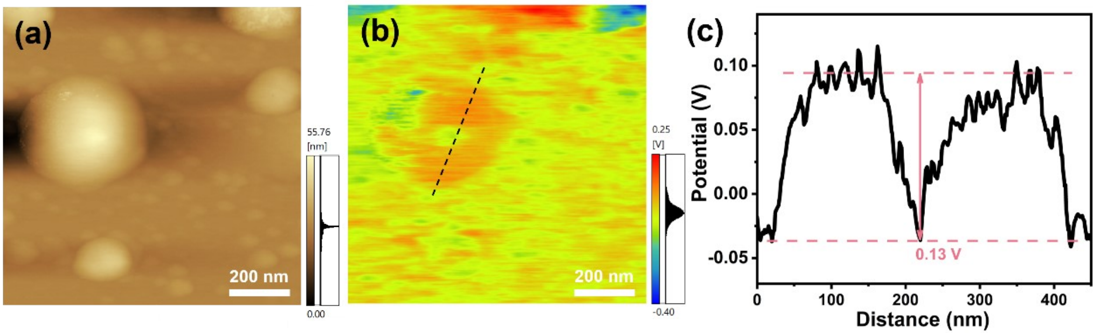

Fig. S12. (a) AFM image; (b) KPFM surface potential distribution; (c) corresponding line scanning of KPFM surface potential of CFO-E2

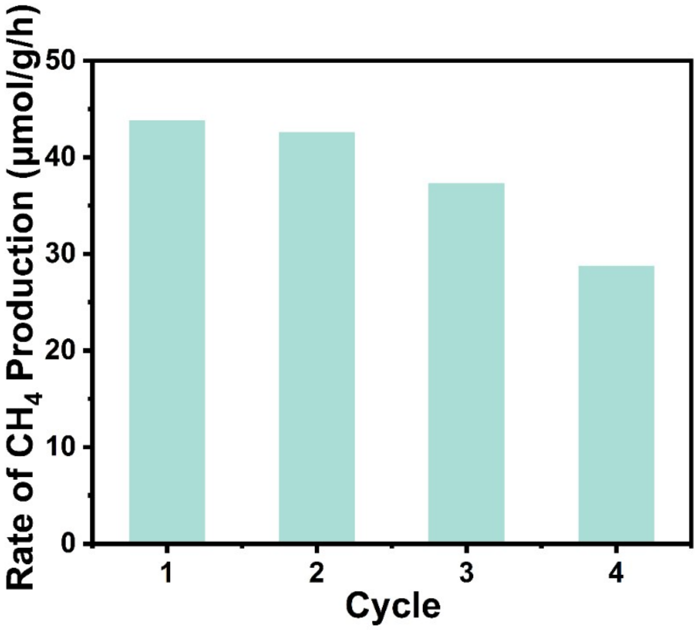

Fig. S13. The recycling performance of CFO-E2 in photocatalytic CO_2 reduction reaction.

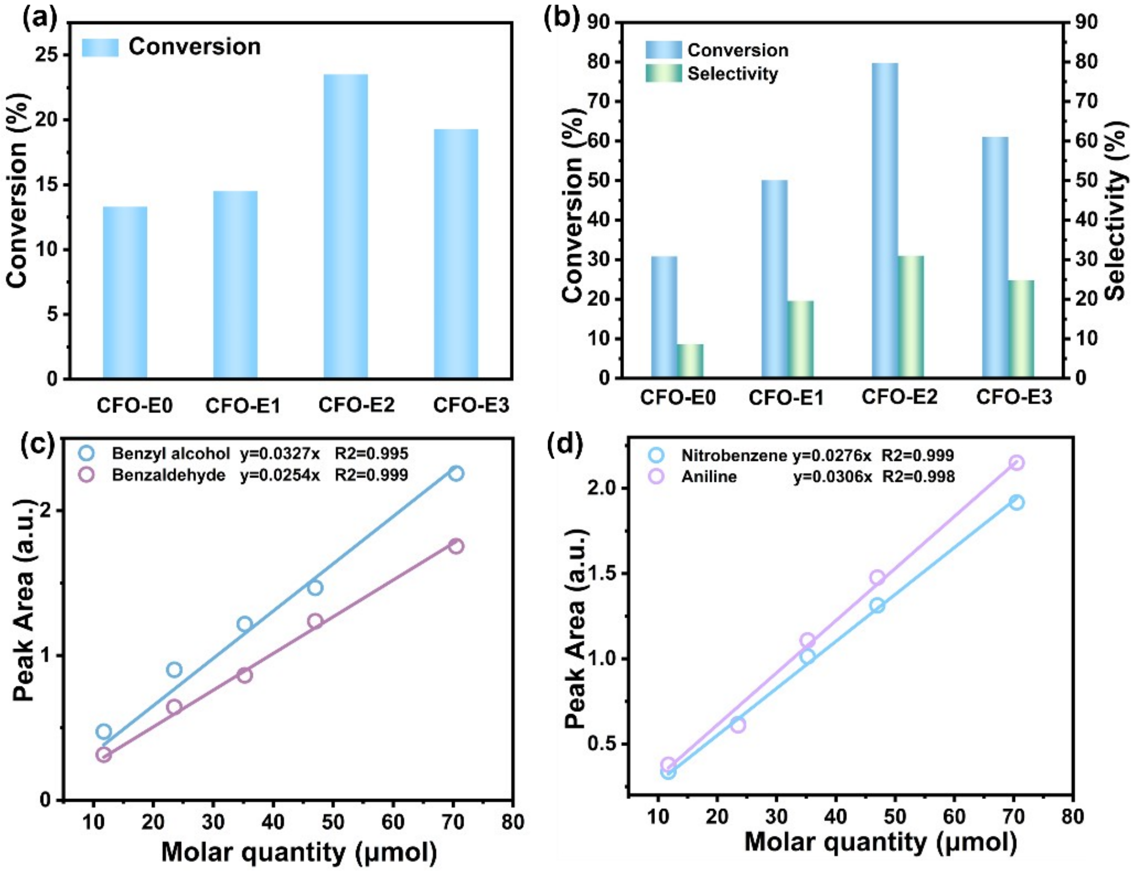

Fig. S14. (a) Comparison of catalytic activity of different samples in photocatalytic benzyl alcohol oxidation; (b) Conversion and selectivity of CFO (E0-E3) in photocatalytic nitrobenzene reduction reactions; (c) Standard curves for benzyl alcohol and nitrobenzene; (d) Standard curves for nitrobenzene and aniline.

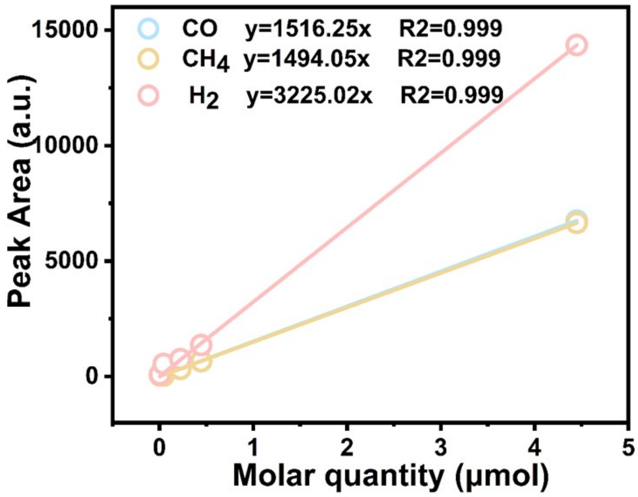

Fig. S15. External standard calibration curve used for calculation of CO, CH_4 and H_2, detected by GC.

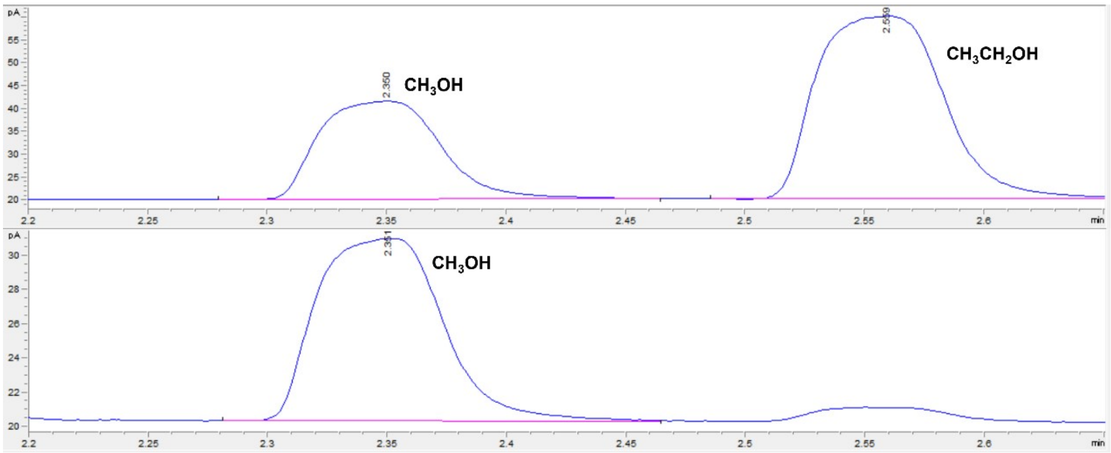

Fig. S16. (a) GC spectrum of CH_3OH and CH_3CH_2OH; (b) GC spectrum of CH_3OH generated during the photocatalytic CO_2 reduction process of CFO-E2.

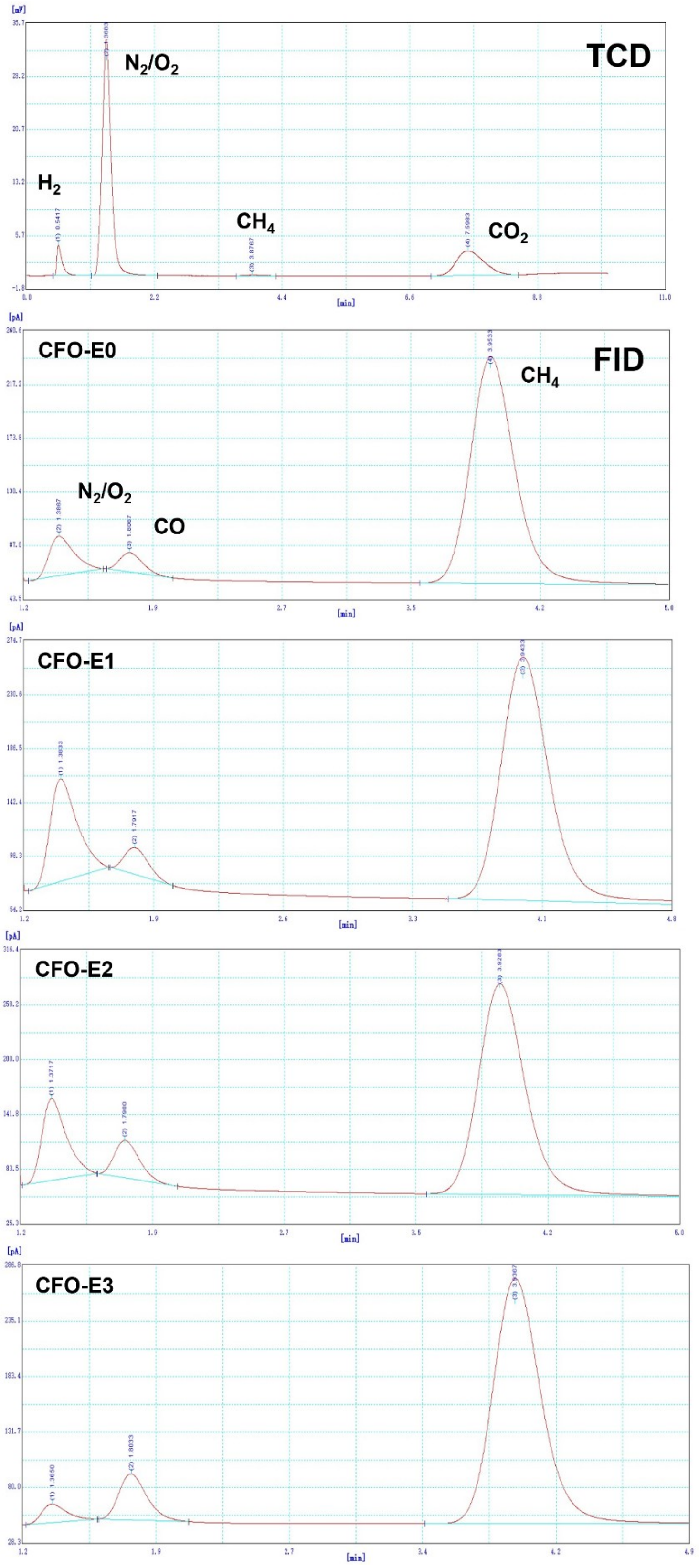

Fig. S17. The GC spectra of CO and CH_4 produced during the photocatalytic CO_2 reduction process of CFO-E0 to CFO-E3.

Table S1. The ratio of 2H (space group: *P*6_3*/mmc*) phases and 3R (space group: *R*$\bar{3}$*m*) phase of $CuFeO_2$ materials.

Sample	Ratio of *P*6_3*/mmc*	Ratio of *R*$\bar{3}$*m*
CFO-E0	36.48%	63.52%
CFO-E2	44.98%	55.02%

Table S2. Specific surface area, pore volume, and average pore size of CFO-E0 and CFO-E2.

Samples	Specific surface area (m^2/g)	Pore volume (cm^3/g)	Pore size (nm)
CFO-E0	3.592	0.021	4.17
CFO-E2	5.313	0.039	3.18

Table S3. Defective oxygen content of CFO obtained by XPS spectral fitting of Ols.

Sample	Lattice O (%)	Defect O (%)	Absorbed O (%)
CFO-E0	64.46	25.77	8.77
CFO-E2	65.69	29.48	5.04

Table S4. Fitting results of Nyquist plots for samples.

Sample	R_s	C_{bulk}	R_{trap}	C_{ss}	R_{ct}
CFO-E0	52.97	8.59×10^{-7}	4437	2.4×10^{-6}	8.76×10^{5}
CFO-E1	53.86	2.3×10^{-6}	1083	1.86×10^{-6}	3.73×10^{5}
CFO-E2	38.34	1.52×10^{-5}	174.3	2.37×10^{-5}	981.5
CFO-E3	39.03	2.27×10^{-6}	5.83×10^{4}	2.52×10^{-6}	8.36×10^{5}

Table S5. The average fluorescence intensity of CFO-E0 and CFO-E2 in 1 μM resazurin (a、d).

Sample	1 μM resazurin
CFO-0	49352
CFO-2	58520

Table S6. The average fluorescence intensity of CFO-E2(Fig. S8) in 1 µM resazurin (a)-(h) and 1 µM amplex red (a)-(f).

Intensity	4.0	6.0	8.0
1 µM amplex red	25957	33421	49713
1 µM resazurin	47868	49703	53776

Table S7. Photocatalytic CO_2 reduction products and selective calculation.

Sample	CO (µmol)	CH_4 (µmol)	CH_3OH (µmol)	Selectivity of CO (%)	Selectivity of CH_4 (%)	Selectivity of CH_3OH (%)
CFO-E0	0.06	2.03	0.29	2.50	85.4	12.1
CFO-E1	0.09	2.24	0.31	3.60	84.6	11.8
CFO-E2	0.37	2.63	0.37	11.0	78.0	11.0
CFO-E3	0.22	2.55	0.20	7.50	85.7	6.8

The selectivity calculation formula for photocatalytic CO_2 reduction products is[1]:

$$Selectivity(\%) = \frac{n(Molar\ quantity\ of\ product)}{n(Total\ molar\ amount\ of\ all\ products)}$$

Table S8. Comparison of photocatalytic CO_2 reduce performance over various photocatalysts and reaction conditions reported in reference.

Photocatalyst	Light source	Condition	Products	Yield
Cu-SA-CO [2]	300 W Xe lamp	CO_2, H_2O vapor	CH_4	58.5 μmol/(g·h)
In_2S_3/In_2O_3 [3]	300 W Xe lamp ($\lambda > 420$ nm)	CO_2 saturated solution (Na_2CO_3 + 0.5 M H_2SO_4)	CO CH_4	2.8 μmol/(g·h) 16.52 μmol/(g·h)
Mn/Co_3O_4 [4]	300 W Xe lamp	CO_2, H_2O vapor	CH_4	23.4 μmol/ (g·h)
Cu_{1+NCs}/BT [5]	300 W Xe lamp	CO_2, H_2O vapor	CO CH_4	2 μmol/(g·h) 19.63 μmol/(g·h)
$PW_9/g\text{-}C_3N_4$ [6]	300 W Xe lamp	CO_2, H_2O vapor	CO CH_4	39.9 μmol/(g·h) 40.8 μmol/(g·h)
U2-PHI [7]	300 W Xe lamp	CO_2, H_2O vapor	CO CH_4	26.3 μmol/(g·h) 52.8 μmol/(g·h)
$Ru_{0.88}Co_{0.12}/TiO_2$ [8]	300 W Xe lamp	CO_2, H_2O vapor	CH_4	191 mmol/(g·h)
Au/TZO [9]	300 W Xe lamp	CO_2 bubble CH_3CN/water/TEOA solution	H_2 CO CH_4 C_2H4 C_2H6	271.6 μmol/(g·h) 260.6 μmol/(g·h) 10.6 μmol/(g·h) 6.8 μmol/(g·h) 4.05 μmol/(g·h)
Ov-BC 2 [10]	300 W Xe lamp	CO_2, H_2O vapor	CH_4	28.5 μmol/(g·h)
$Vo\text{-}Nb_2O_5$ [11]	300 W Xe lamp	CO_2, H_2O vapor	CO CH_4	4.3 μmol/(g·h) 19.14 μmol/(g·h)
Pt@Def-CN [12]	300 W Xe lamp	CO_2, H_2O vapor	CH_4	6.3 μmol/(g·h)
$Sr_{0.8}Bi_{0.2}Ti_{0.8}M_{0.2}O_3$ [13]	300 W Xe lamp	CO_2, H_2O vapor	CO CH_4	3.3 μmol/(g·h) 30.6 μmol/(g·h)
$ZnIn_2S_4/Cu_{1.81}S$ [14]	300 W Xe lamp	CO_2, H_2O vapor	CH_4	23.4 μmol/(g·h)
PNCO 2 [15]	300 W Xe lamp	CO_2, H_2O vapor	CH_4	52.4 μmol/(g·h)
2Cu-ZISF [16]	400-700 nm Xe lamp	CO_2, H_2O vapor	H_2 CO CH_4	2.55 μmol/(g·h) 2.38 μmol/(g·h) 22.27 μmol/(g·h)
Pd_4/SnO_2@rGO [17]	300 W Xe lamp	CO_2 bubble CH_3CN/water/TEOA solution	CH_4	77.8 μmol/(g·h)
Ga_2S_3/CuS [18]	300 W Xe lamp	CO_2 saturated solution (Na_2CO_3 + 0.5 M H_2SO_4)	CH_4	18.8 μmol/(g·h)
$g\text{-}C_3N_4/CuFe_2O_4/ZnInS_4$ [19]	350 W Xe lamp	CO_2, H_2O vapor	CH_4	267.4 μmol/(g·h)
ZZ/Ag-Pt [20]	300 W Xe lamp	CO_2, H_2O vapor	CH_4	16.23 μmol/(g·h)

Table S9. The comparison on etching process between the strategy in this work and those reported in the literature.

Materials	Etching reagent	Applications	Benefits
This work	HCl	CO_2 reduction	Facet junctions
In_2O_3 [21]	K_2PdCl_4（pH=3.84）	CH_4 conversion	Oxygen vacancies
TiO_2@graphene[22]	HCl	RhB degradation	Facets engineering
tZIF-67 [23]	Cyanuric acid	Hydrogen evolution	Surface functionalization
Bi_2WO_6 [24]	NaOH	Bisphenol A degradation	Tungsten and oxygen vacancies
Bi_2WO_6 [25]	NaOH	Sulfamethoxazole degradation	Oxygen vacancies
ZnCr-LDH [26]	NaOH	N_2 reduction	Oxygen vacancies
C_3N_4 [27]	KOH	Overall water splitting	Nitrogen vacancies
$Bi_{19}Br_3S_{27}$ [28]	NaOH	CO_2 reduction	Br and S dual-vacancies
Bi_2MoO_6 [29]	NaOH	Nitrogen fixation	Oxygen vacancies

REFERENCES

1 Y. Gan, M. Huang, F. Yu, X. Yu, Z. He, J. Liu, T. Lin, Y. Dai, Q. Niu and L. Zhong, Highly Selective Photocatalytic Methane Oxidation to Methanol Using CO2 as a Soft Oxidant, *ACS Sustainable Chem. Eng.*, 2023, **11**, 5537–5546.

2 W. Zhang, C. Deng, W. Wang, H. Sheng and J. Zhao, Achieving Almost 100% Selectivity in Photocatalytic CO_2 Reduction to Methane via In-Situ Atmosphere Regulation Strategy, *Advanced Materials*, 2024, **36**, 2405825.

3 K. Lai, Y. Sun, N. Li, Y. Gao, H. Li, L. Ge and T. Ma, Photocatalytic CO_2 -to-CH_4 Conversion with Ultrahigh Selectivity of 95.93% on S-Vacancy Modulated Spatial In_2 S_3 /In_2 O_3 Heterojunction, *Adv Funct Materials*, 2024, **34**, 2409031.

4 M. Li, S. Wu, D. Liu, Z. Ye, L. Wang, M. Kan, Z. Ye, M. Khan and J. Zhang, Engineering Spatially Adjacent Redox Sites with Synergistic Spin Polarization Effect to Boost Photocatalytic CO2 Methanation, *J. Am. Chem. Soc.*, 2024, **146**, 15538–15548.

5 M. Zhang, Y. Mao, X. Bao, P. Wang, Y. Liu, Z. Zheng, H. Cheng, Y. Dai, Z. Wang and B. Huang, Promoting Photocatalytic CO_2 Methanation by the Construction of Cooperative Copper Dual-Active Sites, *ACS Catal.*, 2024, **14**, 5275–5285.

6 Q. Zhu, Z. Li, T. Zheng, X. Zheng, S. Liu, S. Gao, X. Fu, X. Su, Y. Zhu, Y. Zhang and Y. Wei, High-Selectivity Tandem Photocatalytic Methanation of CO2 by Lacunary Polyoxometalates-Stabilized *CO Intermediate, *Angewandte Chemie International Edition*, 2024, **n/a**, e202413594.

7 J. Wu, K. Li, B. Zhou, R. Li, S. Yan, J. Liu, H. Shi, C. Song and X. Guo, Bottom-Up Strategy to Enhance Long-Range Order of Poly(Heptazine Imide) Nanorods for Efficient Photocatalytic CO2 Methanation, *Angewandte Chemie International Edition*, 2024, **n/a**, e202421263.

8 Y. Tang, H. Wang, C. Guo, Z. Yang, T. Zhao, J. Liu, Y. Jiang, W. Wang, Q. Zhang, D. Wu, Y. Zhao, X.-D. Wen and F. Wang, Ruthenium–Cobalt Solid-Solution Alloy Nanoparticles for Enhanced Photopromoted Thermocatalytic CO2 Hydrogenation to Methane, *ACS Nano*, 2024, **18**, 11449–11461.

9 N.-Y. Huang, B. Li, D. Wu, Z.-Y. Chen, B. Shao, D. Chen, Y.-T. Zheng, W. Wang, C. Yang, M. Gu, L. Li and Q. Xu, Crystal Engineering of MOF-Derived Bimetallic Oxide Solid Solution Anchored with Au Nanoparticles for Photocatalytic CO2 Reduction to Syngas and C2 Hydrocarbons, *Angewandte Chemie International Edition*, 2024, **63**, e202319177.

10 J. Fan, L. Shi, H. Ge, J. Liu, X. Deng, Z. Li and Q. Liang, Regulating the Oxygen Vacancy on Bi_2 MoO_6 /Co_3 O_4 Core-Shell Nanocage Enables Highly Selective CO_2 Photoreduction to CH_4, *Adv Funct Materials*, 2025, **35**, 2412078.

11 J. Wu, J. Zhu, W. Fan, D. He, Q. Hu, S. Zhu, W. Yan, J. Hu, J. Zhu, Q. Chen, X. Jiao and Y. Xie, Selective Photoreduction of CO2 to CH4 Triggered by Metal-Vacancy Pair Sites, *Nano Lett.*, 2024, **24**, 696–702.

12 X. Shi, Y. Huang, Y. Bo, D. Duan, Z. Wang, J. Cao, G. Zhu, W. Ho, L. Wang, T. Huang and Y. Xiong, Highly Selective Photocatalytic CO_2 Methanation with Water Vapor on Single-Atom Platinum-Decorated Defective Carbon Nitride, *Angew Chem Int Ed*, 2022, **61**, e202203063.

13 Y. Gao, M. Zhang, Y. Jin, Y. Mao, W. Wang and Z. Song, Construction of Dual Active Sites in Perovskite Oxide for Targeted Photocatalytic CO2 Reduction to CH4, *ACS Catal.*, 2024, **14**, 10746–10759.

14 Y. Sun, K. Lai, X. Shi, N. Li, Y. Gao and L. Ge, Regulating metal cation Cu vacancies on ZnIn2S4/Cu1.81S to achieve high selectivity for the photocatalytic reduction of CO2 to CH4, *Applied Catalysis B: Environment and Energy*, 2025, **365**, 124907.

15 J. Li, Y. Li, M. Han, Y. Yamauchi and G. Zhang, Enhanced photocatalytic CO2 reduction to CH4 on oxygen vacancy-rich NiCo2O4 with surface pits: Synthesis, DFT calculations, and mechanistic insights, *Chemical Engineering Journal*, 2024, **499**, 156429.

16 Z. Li, J. Xiong, Y. Huang, Y. Huang, G. I. N. Waterhouse, Z. Wang, Y. Mao, Z. Liang and X. Luo, Rational design of spatial charge separation and targeted active site Cu for highly selective photocatalytic CO2 reduction to CH4, *Chemical Engineering Journal*, 2024, **495**, 153310.

17 F. Kong, J. Xie, Z. Lu, J. Hu, Y. Feng and Y. Cao, Regulating CHO* intermediate pathway towards the significant acceleration of photocatalytic CO2 reduction to CH4 through rGO-coated ultrafine Pd nanoparticles, *Chemical Engineering Journal*, 2024, **481**, 148497.

18 Y. Sun, K. Lai, N. Li, Y. Gao and L. Ge, Efficient photocatalytic CO2 reduction to CH4 via electric field-regulated d-band center on Ga2S3/CuS S-type heterojunction interface structures, *Applied Catalysis B: Environment and Energy*, 2024, **357**, 124302.

19 D. Liu, L. Jiang, D. Chen, Z. Hao, B. Deng, Y. Sun, X. Liu, B. Jia, L. Chen and H. Liu, Twin S-Scheme g-C3N4/CuFe2O4/ZnIn2S4 Heterojunction with a Self-Supporting Three-Phase System for Photocatalytic CO2 Reduction: Mechanism Insight and DFT Calculations, *ACS Catal.*, 2024, **14**, 5326–5343.

20 Q. Li, Q. Wang, Y. Zeng, Y. Xu, X.-K. Gu and M. Ding, Ag–Pt Alloy Nanoparticles Modified Zn-Based Nanosheets for Highly Selective CO2 Photoreduction to CH4, *Advanced Functional Materials*, 2024, **n/a**, 2416975.

21 L. Luo, L. Fu, H. Liu, Y. Xu, J. Xing, C.-R. Chang, D.-Y. Yang and J. Tang, Synergy of Pd atoms and oxygen vacancies on In2O3 for methane conversion under visible light, *Nature Communications*, 2022, **13**, 2930.

22 H. Liu, S. Liu, Z. Zhang, X. Dong and T. Liu, Hydrothermal etching fabrication of TiO2@graphene hollow structures: mutually independent exposed {001} and {101} facets nanocrystals and its synergistic photocaltalytic effects, *Scientific Reports*, 2016, **6**, 33839.

23 Z.-X. Cai, Z.-L. Wang, Y.-J. Xia, H. Lim, W. Zhou, A. Taniguchi, M. Ohtani, K. Kobiro, T. Fujita and Y. Yamauchi, Tailored Catalytic Nanoframes from Metal–Organic Frameworks by Anisotropic Surface Modification and Etching for the Hydrogen Evolution Reaction, *Angewandte Chemie International Edition*, 2021, **60**, 4747–4755.

24 X. Zhang, Y. Zhang, H. Li, Y. Wang, M. Xiang, W. Yu, H. Huang and H. Ou, Surface cationic and anionic dual vacancies enhancing photocatalytic activity of Bi2WO6, *Applied Surface Science*, 2022, **602**, 154311.

25 H. Ma, W. Yang, S. Gao, W. Geng, Y. Lu, C. Zhou, J. K. Shang, T. Shi and Q. Li,

Superior photopiezocatalytic performance by enhancing spontaneous polarization through post-synthesis structure distortion in ultrathin Bi2WO6 nanosheet polar photocatalyst, *Chemical Engineering Journal*, 2023, **455**, 140471.

26 Y. Zhao, L. Zheng, R. Shi, S. Zhang, X. Bian, F. Wu, X. Cao, G. I. N. Waterhouse and T. Zhang, Alkali Etching of Layered Double Hydroxide Nanosheets for Enhanced Photocatalytic N2 Reduction to NH3, *Advanced Energy Materials*, 2020, **10**, 2002199.

27 Y. Shao, X. Hao, S. Lu and Z. Jin, Molten salt-assisted synthesis of nitrogen-vacancy crystalline graphitic carbon nitride with tunable band structures for efficient photocatalytic overall water splitting, *Chemical Engineering Journal*, 2023, **454**, 140123.

28 J. Li, W. Pan, Q. Liu, Z. Chen, Z. Chen, X. Feng and H. Chen, Interfacial Engineering of Bi19Br3S27 Nanowires Promotes Metallic Photocatalytic CO2 Reduction Activity under Near-Infrared Light Irradiation, *J. Am. Chem. Soc.*, 2021, **143**, 6551–6559.

29 G. Li, W. Yang, S. Gao, Q. Shen, J. Xue, K. Chen and Q. Li, Creation of rich oxygen vacancies in bismuth molybdate nanosheets to boost the photocatalytic nitrogen fixation performance under visible light illumination, *Chemical Engineering Journal*, 2021, **404**, 127115.